

Supplementary Materials for

Nano-kirigami with giant optical chirality

Zhiguang Liu, Huifeng Du, Jiafang Li*, Ling Lu, Zhi-Yuan Li*, Nicholas X. Fang*

*Corresponding author. Email: jiafangli@aphy.iphy.ac.cn (J.L.); phzyli@scut.edu.cn (Z.-Y.L.); nicfang@mit.edu (N.X.F.)

Published 6 July 2018, *Sci. Adv.* **4**, eaat4436 (2018)

DOI: 10.1126/sciadv.aat4436

The PDF file includes:

Section S1. Mechanical modeling

Section S2. Optical modeling

Section S3. Extension of nano-kirigami to other materials and geometries

Fig. S1. Illustration of the overhead ion beam blocking and comparison between local and global ion beam irradiation.

Fig. S2. Exotic 3D structures fabricated by nano-kirigami.

Fig. S3. SRIM software simulation results.

Fig. S4. Ion beam dosage test.

Fig. S5. Schematic of the bottom layer under elastoplastic deformation.

Fig. S6. Comparison between web-like structures of different topographies after nano-kirigami.

Fig. S7. Origin of the chirality in 3D pinwheel structures.

Fig. S8. Structural designs for optical chirality.

Fig. S9. Numerical calculations and comparison with experiments.

Fig. S10. Extension of nano-kirigami to other platforms.

Other Supplementary Material for this manuscript includes the following:

(available at advances.sciencemag.org/cgi/content/full/4/7/eaat4436/DC1)

Movie S1 (.avi format). Nano-kirigami of different structures by programming ion beam irradiation in one step.

Movie S2 (.avi format). Upward and downward buckling with nano-kirigami.

Movie S3 (.avi format). Structural evolution of different web-like structures under nano-kirigami.

Movie S4 (.avi format). Simultaneous upward buckling of an array of pinwheel structures.

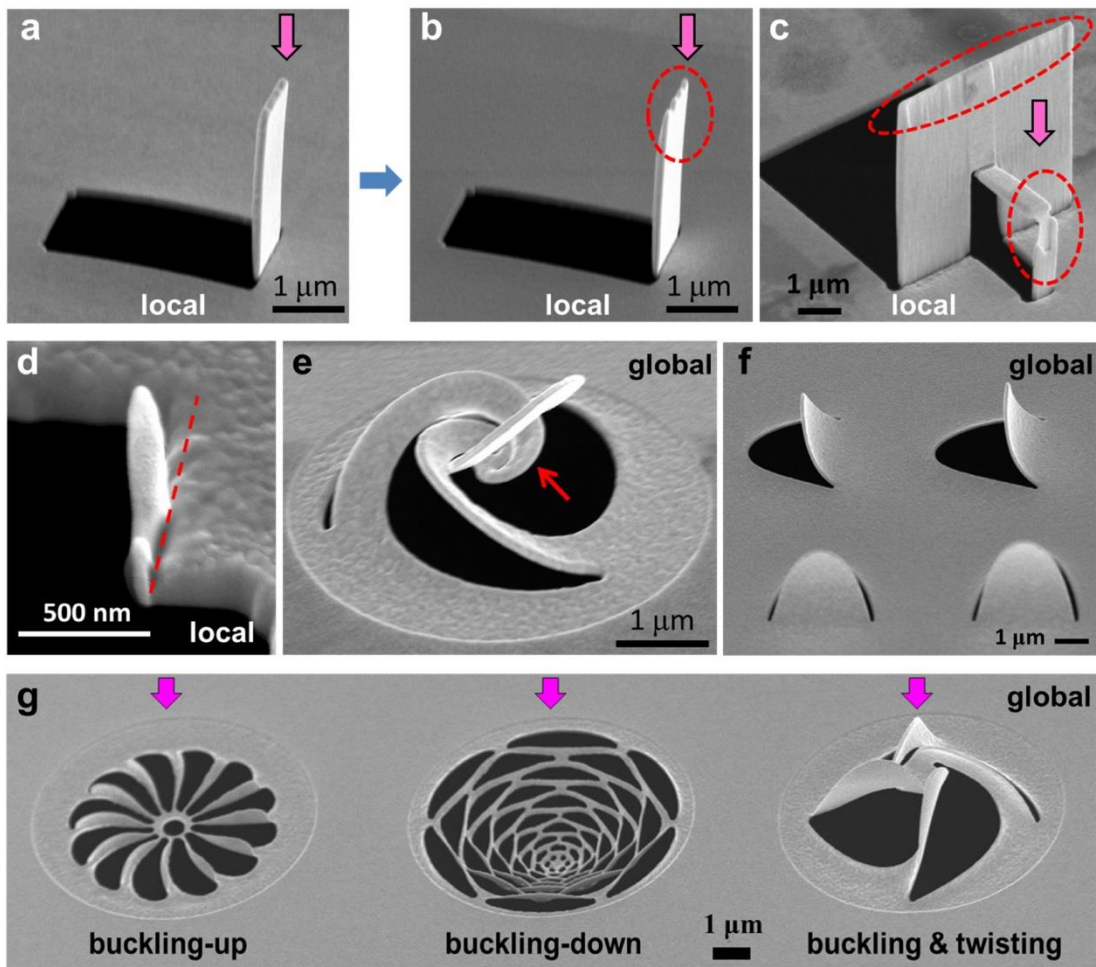


Fig. S1. Illustration of the overhead ion beam blocking and comparison between local and global ion beam irradiation. (a to c) SEM images of gold micro-strips fabricated by local irradiation (line-scanning mode) with gallium-based focused ion beam (FIB), which induces zero global curvatures except at the abruptly localized regions (the ion-beam irradiation regions). FIB is incident from the normal direction, as noted by the vertical arrows. When the structures are folded with nearly 90 degrees, the over-head ion beams are partly blocked by the upright structures, which causes the destroys of the structures, as noted by the dashed ellipses in figs. S1b-1c. (d) Cross-section SEM image of an upward folded structure after cut by FIB. The dashed line indicates the area where coalescence occurs around the vacancies induced by ion-beam irradiation. (e, f) SEM images of a twisted triple Fibonacci spirals and tongue-like structures fabricated with global ion-beam irradiation. Non-zero curvatures and cross-over structures (indicated by the red arrow) such as the twisted spirals in (e) are impossible to be fabricated with the local irradiation method, reflecting the uniqueness of the global ion-beam irradiation induced nano-kirigami. (g) SEM images of a propeller-like structure, a micro-dome and a pinwheel structure fabricated with nano-kirigami in the same gold film, in which the buckling-up, buckling-down and buckling&twisting transformation features are clearly seen. Ion beams are incident from the normal direction (noted by the arrows). Therefore, for the micro-dome structure, this is a buckling-down process when it is seen from the ion-beam illumination direction.

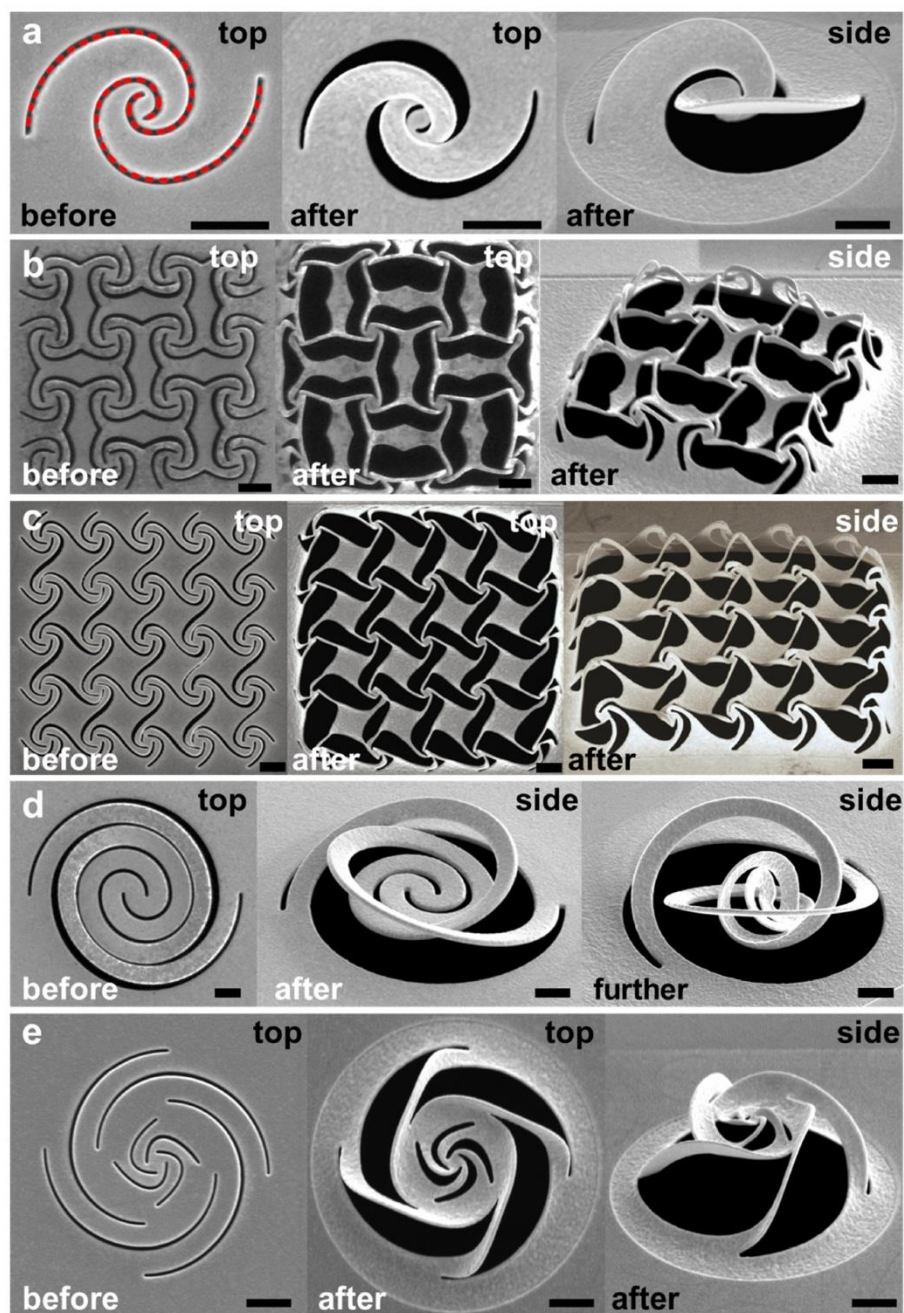


Fig. S2. Exotic 3D structures fabricated by nano-kirigami. Top-view and side-view scanning electron/ion microscope (SEM) images of the typical structures before and after global ion-beam irradiation. **(a)** Combined double Fibonacci spirals. **(b)** and **(c)** Window-decoration-type interconnected nano-barriers. **(d)** A deformable spiral before and after global ion-beam illumination with different ion doses. **(e)** A combined spiral heterostructure. Scale bars: 1 μm .

Section S1. Mechanical modeling

1.1 The modified bilayer model

Although the effects of focused ion beam (FIB) irradiation on nanoscale thin film have been studied (19, 24), the complete physical mechanisms of how the FIB-induced structural changes are related to material properties and modifications at continuum-mechanics level is still unclear. One reason is that previous theories on membrane folding and unfolding were based on purely elastic material assumptions like Stoney formula (19, 24). They were found inadequate when modeling the constrained film buckling with finite deformation as several key requirements of implementing Stoney formula are not satisfied, including constant radius of curvature and linear elasticity.

We hereby develop a comprehensive mechanics model which characterizes the Au film as a bilayer elastoplastic thin sheet with FIB-induced residual stress gradient, which inherits the bilayer feature of previous models using the well-known Stoney Equation (24), along with explicit forms of distribution of residual stress inside the bilayer and proper justification. This bilayer assumption is well accounted for as the gallium ion implantation depth is found around 20 nm from the top surface and therefore doesn't penetrate the whole Au film in this study, which is predicted by the simulations in fig. S3.

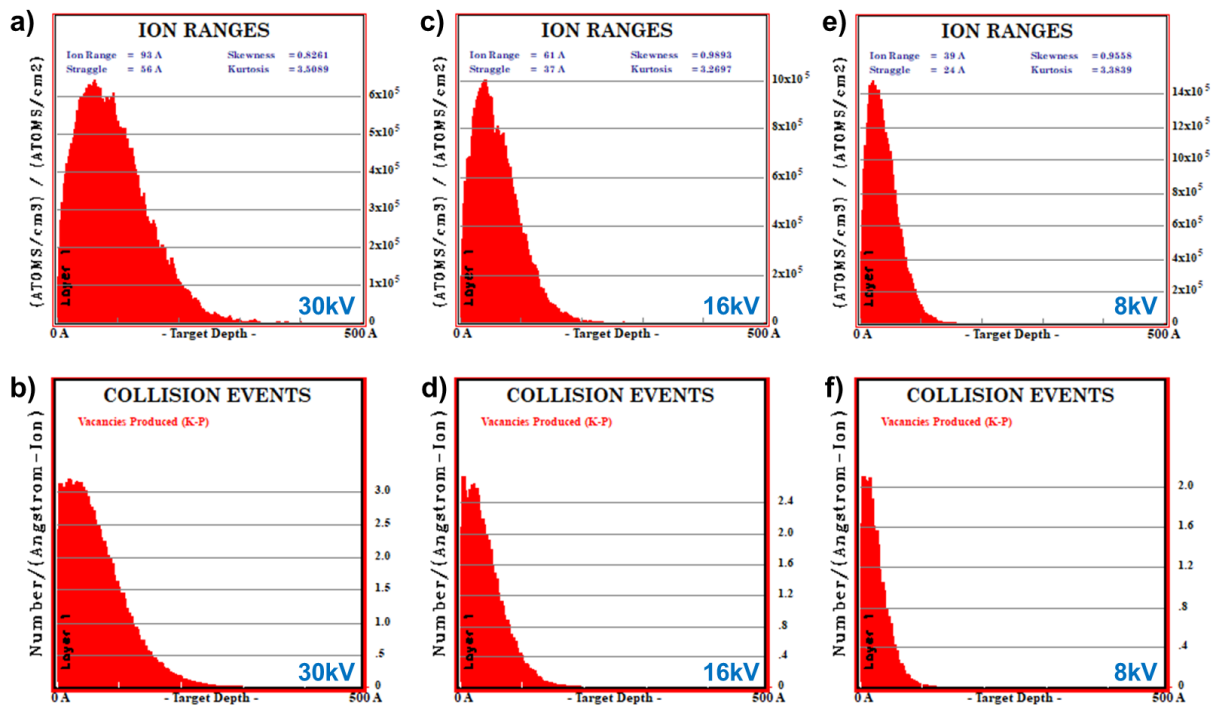


Fig. S3. SRIM software simulation results. SRIM plot of gallium ion concentration and vacancy density as a function of Au film depth under ion beam acceleration voltage of 30, 16 and 8 kV, respectively. The ion range is 9.3, 6.1 and 3.9 nm, respectively, and the penetration depth is less than 20 nm in all cases, both of which decrease with the reduction of acceleration voltage. SRIM software can be available from <http://www.srim.org/>.

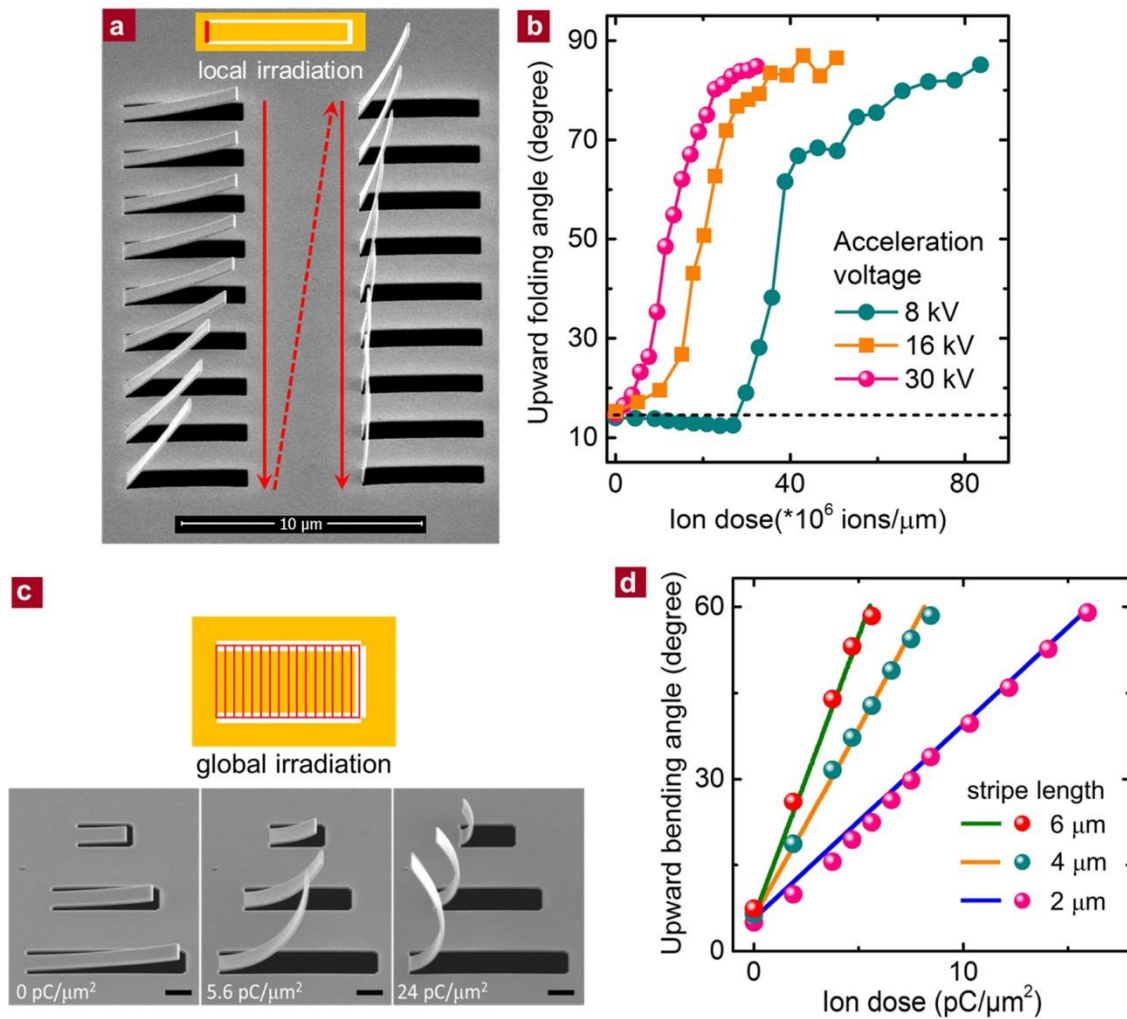


Fig. S4. Ion beam dosage test. (a) Side-view SEM images of upward folded micro-strips ($\sim 1 \mu\text{m} \times 5 \mu\text{m}$) after local irradiation (scanning along the red line schematically shown in the inset) with Ga^+ beams with different doses under acceleration voltage of 30 kV. The scanned lines are $\sim 1 \mu\text{m}$ in length and the linewidth is about 30 nm. The red arrows point out the increasing direction of illumination dosages. (b) Measured upward folding angle as a function of ion dose under acceleration voltage of 8, 16 and 30 kV, respectively. It can be seen that Ga^+ implantation induced compressive stress exerts negligible effect in these cases since all of the stripes are upward folded. (c) SEM images of the strips under global ion-beam irradiation with increased dose as noted. The lengths of the 1- μm -wide suspended stripes are 6, 4 and 2 μm , respectively. The FIB irradiation areas cover the whole suspended stripe, as the grid area illustrated on the top. Scale bars: 1 μm . (d) Measured upward bending angle (solid circles) of micro-strips as a function of the ion dose under global ion-beam irradiation with acceleration voltage of 30 kV, which agree excellently with the calculations by using our mechanical model (solid lines) under low-dose irradiation. One may notice the warps of the stripes under high-dose irradiation (24 $\text{pC}/\mu\text{m}^2$) in (c), which result in the deviation from calculation due to the decrease of the effective irradiation areas. Nevertheless, at the initial stage and with relatively low-dose irradiation that mostly employed in our nano-kirigami method, the calculations with our mechanical model are well consistent with the experimental results, as plotted in (d).

In this model, the most affected top layer of the film undergoes significant changes in crystallographic structures and possible amorphization where motions of dislocations happen at the crystallographic slip planes. The combination of collision-generated vacancies and ion-implantation effects produce tensile-like residual stress throughout the entire scan (fig. S4), and the top amorphous layer subsequently contracts to release the residual stress until new equilibrium is achieved. The irreversible yielding strain associated with

large deformation of folding films in the top layer cannot be neglected, which is evident from the fact that free standing cantilever didn't completely unfold to its initial state after annealing (19). Due to the inelastic nature of deformation in this layer, the residual stress is characterized with an elastic-perfectly plastic model with constant yielding stress as illustrated in Fig. 2a, and a fully plastic zone is expected when the accumulative ion concentration is building up to achieve membrane folding and large global buckling of the 3D structure. The thickness of this amorphous layer is determined by the acceleration voltage and independent of beam current during FIB exposure (24), and this explains why the critical values of ion doses upon which the folding angle of a stripe begins to increase have strong dependence on the acceleration voltages, as verified in fig. S4b.

In comparison, the less affected bottom layer of Au film experiences less amorphization and deforms elastically as the affected top layer contracts due to the tensile residual stress. As the microscopic structures of polycrystalline Au in the bottom layer remain largely intact and ordered than the top layer, a dislocation is less likely to move along crystallographic slip plane and results in higher yield strength of macroscopic material property. Consequently, the stress remains lower than the yielding point and the top-layer contraction induced global bending will generally produce non-uniform stress distribution with constant gradient (i.e. linear form) across the thickness of membrane (detailed justifications will be discussed in next section).

1.2 Distribution of stress in the bottom layer

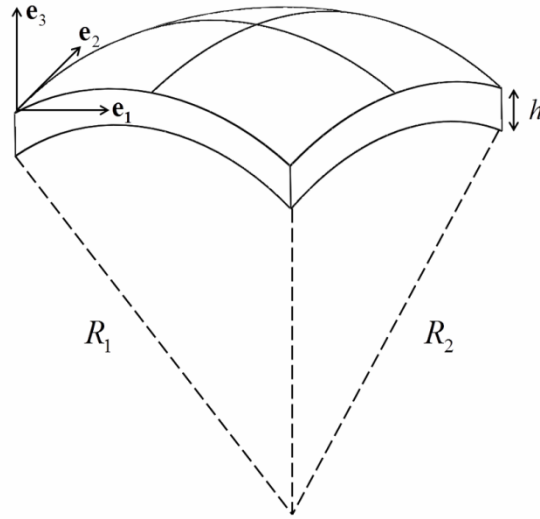


Fig. S5. Schematic of the bottom layer under elastoplastic deformation.

To identify the form of the stress distribution inside the bottom layer under elastoplastic deformation, a schematic of the film is plotted in fig. S5, where the film thickness h in the direction \mathbf{e}_3 is much smaller than the characteristic lengths along the other two edges. In such a case, it could essentially be treated as a thin plate with plane stress conditions applied (21)

$$\sigma_{\alpha\beta} = \sigma_{\alpha\beta}(x_1, x_2), \quad \sigma_{33} = \sigma_{13} = \sigma_{23} = 0 \quad (1)$$

where the subscripts α, β range over the values 1 and 2.

For three-dimensional homogeneous, isotropic, linear elastic body, one obtains

$$\varepsilon_{\alpha\beta} = \frac{(1+\nu)}{E} \left(\sigma_{\alpha\beta} - \frac{\nu}{(1+\nu)} (\sigma_{\gamma\gamma}) \delta_{\alpha\beta} \right) \quad (2)$$

with $\varepsilon_{13} = \varepsilon_{23} = 0$, $\varepsilon_{33} = -\frac{\nu}{E} \sigma_{\gamma\gamma} = -\frac{\nu}{E} (\sigma_{11} + \sigma_{22})$.

When expressed in terms of strains, the plane stress could be expressed by a constitutive equation

$$\sigma_{\alpha\beta} = \frac{E}{(1+\nu)} \left(\varepsilon_{\alpha\beta} + \frac{\nu}{(1-\nu)} (\varepsilon_{\gamma\gamma}) \delta_{\alpha\beta} \right) \quad (3)$$

The radii of curvature (R_1, R_2) in fig. S5 are related with the displacement field $\mathbf{u} = (u_1, u_2, u_3)$ by

$$\frac{1}{R_1} = \frac{u_{3,11}}{(1+u_{3,1}^2)^{3/2}}, \quad \frac{1}{R_2} = \frac{u_{3,22}}{(1+u_{3,2}^2)^{3/2}} \quad (4)$$

Assuming plane cross-section, the kinematic relationships that relate strains to displacement are expressed as

$$\begin{aligned} \varepsilon_{11} &= \frac{e}{R_1} - \frac{x_3}{R_1} = (-x_3 + e) \frac{u_{3,11}}{(1+u_{3,1}^2)^{3/2}} \\ \varepsilon_{22} &= \frac{e}{R_2} - \frac{x_3}{R_2} = (-x_3 + e) \frac{u_{3,22}}{(1+u_{3,2}^2)^{3/2}} \\ \varepsilon_{33} &= -\frac{\nu}{(1-\nu)} (\varepsilon_{11} + \varepsilon_{22}) = \frac{\nu}{(1-\nu)} (x_3 - e) \left(\frac{u_{3,11}}{(1+u_{3,1}^2)^{3/2}} + \frac{u_{3,22}}{(1+u_{3,2}^2)^{3/2}} \right) \end{aligned} \quad (5)$$

Substituting Eq.(5) back into the constitutive equation Eq.(3), one gets

$$\begin{aligned} \sigma_{11} &= \frac{E}{1-\nu^2} (-x_3 + e) \left(\frac{u_{3,11}}{(1+u_{3,1}^2)^{3/2}} + \nu \frac{u_{3,22}}{(1+u_{3,2}^2)^{3/2}} \right) \\ \sigma_{22} &= \frac{E}{1-\nu^2} (-x_3 + e) \left(\frac{u_{3,22}}{(1+u_{3,2}^2)^{3/2}} + \nu \frac{u_{3,11}}{(1+u_{3,1}^2)^{3/2}} \right) \end{aligned} \quad (6)$$

which is a linear function of the coordinate x_3 along the thickness direction. Therefore, the elastoplastic stress inside the bottom layer keeps a linear distribution across the film thickness.

1.3 Comparison between experimental observations and mechanical modellings

With the above analysis, the ion-beam irradiation induced residual stress within ultra-thin Au film in our modified bilayer model, as illustrated in Fig. 2a, could be simplified as

$$\sigma_{11(22)}^{\text{in-plane}}(x_3) = \begin{cases} \sigma_t = \text{const}, & h_b < x_3 \leq h_b + h_t \\ \sigma_b = \sigma_0^{\text{in-plane}} + kx_3 + o(x_3), & 0 \leq x_3 \leq h_b \end{cases} \quad (7)$$

Here x_3 is the coordinate in the thickness direction (\mathbf{e}_3); h_t and h_b are the thicknesses of top and bottom layers, respectively; σ_t and σ_b are the residual stress in the top and bottom layers, respectively; $\sigma_0^{\text{in-plane}}$ and k are the first-order and second-order coefficient in the asymptotic expansion of stress in the bottom layer with little $o(x_3)$ representing the higher orders (the higher-order term is negligible considering the ultra-small thickness of the films). During the numerical simulations these quantities are treated as fitting parameters when comparing results from computational method with experimental outcomes.

To validate this bilayer model, we first compare the model to experiments with local irradiation induced folding along specific hinge lines (fig. S4a). As shown in fig. S4b, the critical ion dose upon which the upward folding angle of cantilever starts to increase dramatically strongly depends on the acceleration voltage. Although the microscopic physical mechanisms of stress and constitutive relations in the bilayer model differ (19), the curvature of up-folding freestanding film have the same mathematical form if we linearize the radius of curvature expression and assume integral force and momentum freedoms

$$|\kappa| \sim \frac{6(1-\nu)}{E} \sigma^{\text{in-plane, top}} \frac{h_t(h_t + h_b)}{h_b^3} \quad (8)$$

When the ion dose is low, $\sigma_Y^{\text{in-plane, top}}$ doesn't exceed the yield strength of amorphous layer Y_p and the rising stress $\sigma_Y^{\text{in-plane, top}}$ still falls in the elastic regime. At the lowest acceleration voltage tested at 8 kV amorphous

top layer is very thin compared with the bottom layer ($\frac{h_t(h_t + h_b)}{h_b^3} \rightarrow 0$), hence the curvature $|\kappa|$ remains

almost unchanged with increasing stress at low voltage and grows rapidly at higher voltages; after $\sigma_Y^{\text{in-plane, top}}$ reaches the upper bound, the amorphous layer begins to deform plastically with the formation and coalescence of vacancies to initiate the propagation of crack, until the material eventually fails by ductile fracture. New amorphous layer starts to develop on top of previously less affected bottom layer, resulting in decreasing polycrystalline layer thickness h_b and the curvature keeps growing as $\frac{h_t(h_t + h_b)}{h_b^3}$ goes up, which is also

validated by experimental observation of localized thinning and necking at the plastic hinges.

To further demonstrate the feasibility of global deformation and quantitatively relate the model parameters to ion irradiation dose, we conduct global ion-beam illumination over the entire freestanding cantilevers (top of fig. S4c) and compare with simulation results. As shown in fig. S4d, when upward bending is initially triggered by ion beam irradiation, the folding angles increase linearly with irradiation dosages and are well predicted by our model in all cases. This excellent agreement between FEM simulation of our model and experiment in determining the bending-dosage relationship within the linear region suggests our bilayer elastoplastic model successfully recover the physical mechanism of residual stress gradients developed during global ion-beam irradiation, which holds great promise in harnessing the rational design of prescribed cut-and-fold patterns on Au nanofilm to actuate global buckling of thin membranes into complex 3D architectures. These advantages have resulted in excellent agreement between numerical simulations and nano-kirigami experiments, such as those in figs. 2b-2e and Fig. 3d of the main text.

1.4 User-defined subroutines in Abaqus software

The deformed configurations of 3D nano-kirigami architectures were calculated with finite element software SIMULIA Abaqus FEA. However, standard SIMULIA Abaqus FEA doesn't allow non-uniform predefined stress fields in Eq. (7) to be specified directly. Alternatively, the non-uniform predefined stress fields could be equivalently represented by giving the structures an effective thermal expansion and a prescribed inhomogeneous initial temperature field. It should be noted that such an equivalent process is only utilized to produce residual stress at the initial step and has no influence over the structure as deformation propagates.

An exemplary Abaqus UTEMP subroutine is shown below, which represents a piece-wise linear temperature field.

```

SUBROUTINE UTEMP(TEMP,NSECPT,KSTEP,KINC,TIME,NODE,COORDS)
C
  INCLUDE 'ABA_PARAM.INC'
C
  DIMENSION TEMP(NSECPT), TIME(2), COORDS(3)
C

  IF (COORDS(3) .GE. h_b) THEN
    TEMP(1) = T_0
  ELSE

    TEMP(1) = T_1+(T_0-T_1)*(COORDS(3)*k+c)
  END IF

  RETURN
END
```

Here, h_b stands for the inflection point of stress distribution function (see Fig. 2a for illustration), $COORDS(3)$ indicates the coordinate along the thickness of membrane. T_0 and T_1 are temperature values and can be converted to stress values via thermal expansion coefficients specified in the Abaqus input file. k and c are coefficients for the linear part of this stress distribution.

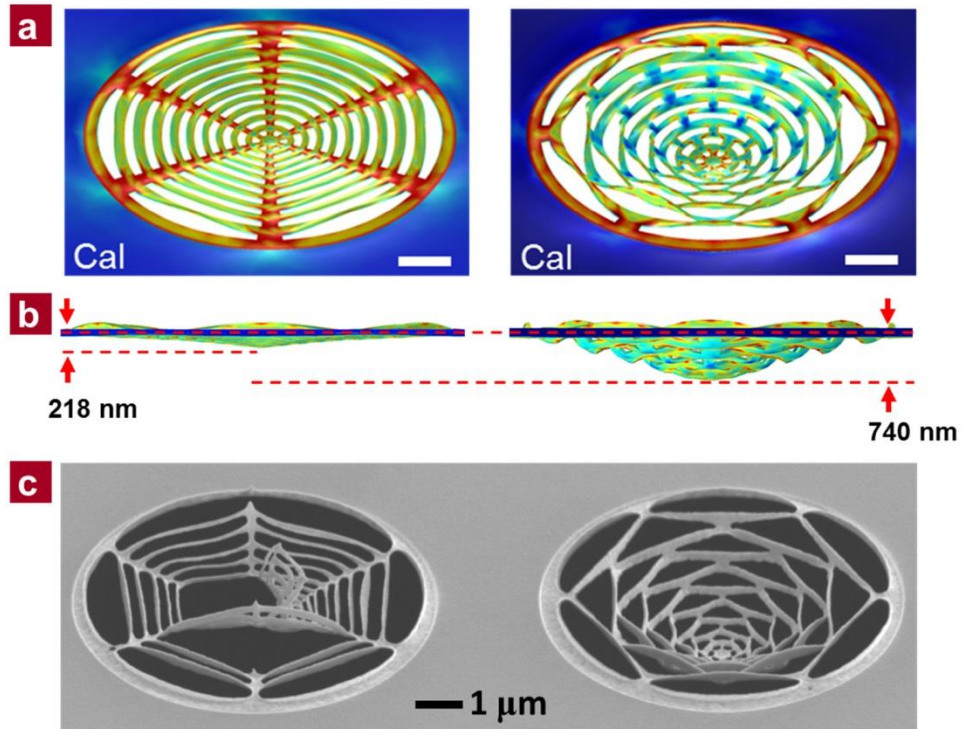


Fig. S6. Comparison between web-like structures of different topographies after nano-kirigami. (a) Perspective-view and (b) front-view of the calculated results of a spider-web-like and a concentric-arc structure under peak residual stress of 4.5 GPa. Due to their different topographies, the equilibrium stresses are localized at apparently different regions, which result in different downward bending (buckling-down) height as noted in (b). It can be seen that the downward buckling of the concentric-arc structure is ~240% larger than that of the spider-web pattern. (c) SEM images of a spider-web-like and a concentric-arc structure after the same ion-beam irradiation with relatively large dose. The radial connection in the spider-web structure is broken while the concentric-arc structure is in good shape. This is because in the spider-web structure, the stress is mainly concentrated on the radial connection parts while the concentric-arc structure shows relative uniform stress distribution. Therefore, when the stress increases to certain stage by adding the ion-beam dose, the radial connection parts will firstly receive the fracture threshold. These results are interesting for the structural optimization of nanoscale web-like structure (26).

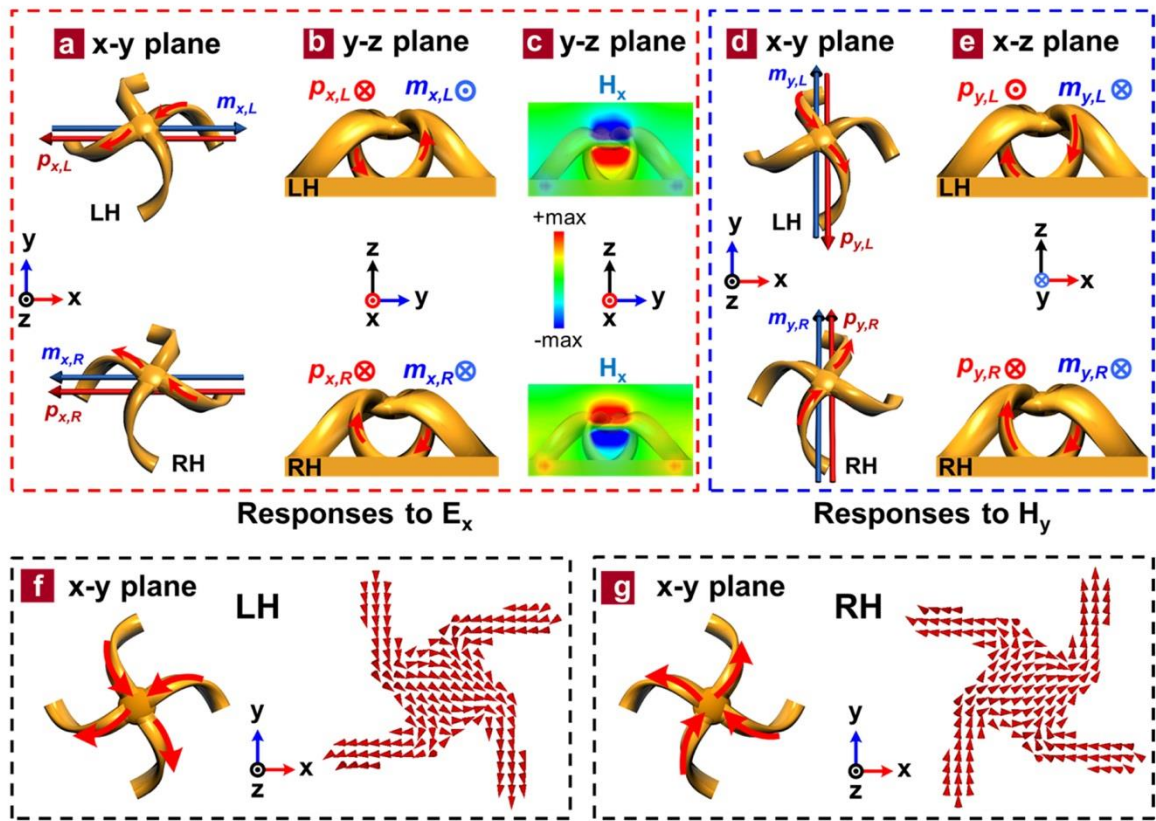


Fig. S7. Origin of the chirality in 3D pinwheel structures. (9, 28, 31). (a and b) Illustration of the responses to the electric field (E_x) of incident light for the left-handed (LH) and right-handed (RH) twisted pinwheels in (a) x-y plane and (b) y-z plane, respectively. (c) Calculated magnetic field (H_x) at wavelength $1.7 \mu\text{m}$ in the y-z plane ($x=0$) under x-polarized excitation for a realistic configuration in figs. S9a-9b. The direction of H_x at center part of the pinwheels agrees well with the illustration in (a) and (b). (d, e) Illustration of the responses to the magnetic field (H_y) of incident light for LH and RH twisted pinwheels in (d) x-y plane and (e) x-z plane, respectively. The direction of induced electric moments $p_{i,j}$ ($i = x$ or y , $j = L$ or R) and magnetic moments $m_{i,j}$ at the center parts are noted by the arrows for LH ($j = L$) and RH ($j = R$) pinwheels, respectively. (f and g) Schematic and calculated electric current density at wavelength $1.7 \mu\text{m}$ in the center parts of (f) LH and (g) RH 3D pinwheels, respectively. It can be seen that the calculated current flows are consistent with the illustration in figs. S7a-S7b and figs. S7d-S7e, respectively. It should be mentioned that similar analysis can also be obtained by treating the 3D pinwheel as two cross-linked and twisted Ω -shape circuits (28) standing onto a metallic hole array.

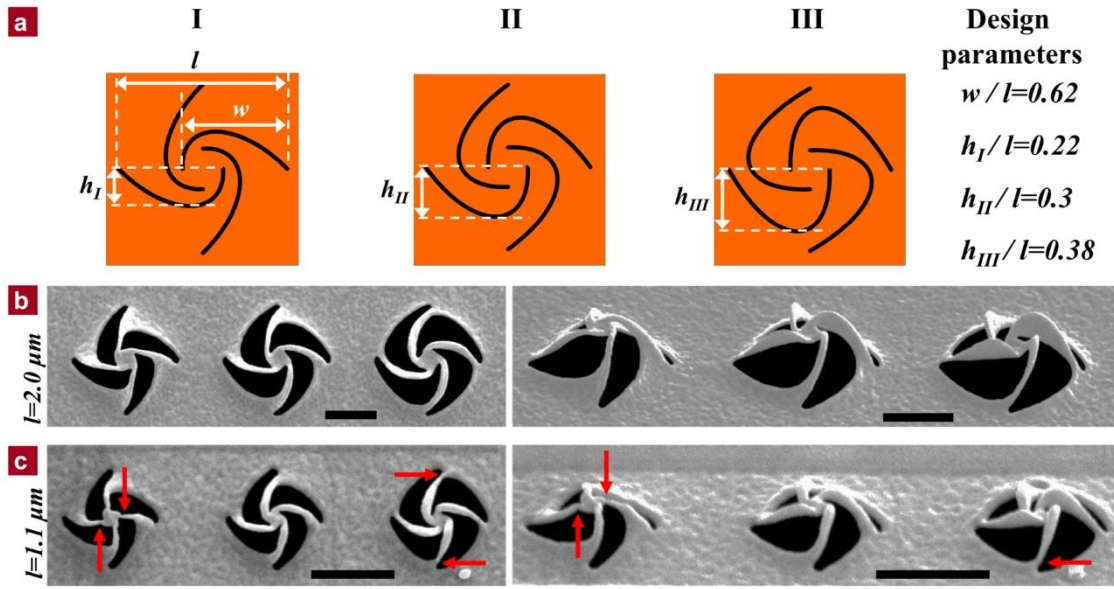


Fig. S8. Structural designs for optical chirality. (a) Schematic designs of three types of 2D spiral patterns with different parameters. The curves are varied based on the type I spiral, in which the subunit curve of each arm is defined by a spindle function of $\rho^2 = w^2 \sin 2\theta$ with $\theta \in [0, \pi/4]$. (b, c) Top-view and side-view SEM images of the 3D pinwheels after global ion-beam irradiation on the 2D spirals with parameters (b) $l=2$ and (c) $1.1 \mu\text{m}$, respectively. As noted by the red arrows, the top ends of the arms in type I and the bottom ends of the arms in type III pinwheels are very thin and fragile upon distortion when the structures are scaled down (l decreased from $2 \mu\text{m}$ to $1.1 \mu\text{m}$). Scale bars: $1 \mu\text{m}$.

Section S2. Optical modeling

The exotic 3D nanostructures enabled by nano-kirigami are complex and irregular in geometries due to their twisting features and atom dislocation process. For example, the 3D pinwheels in Fig. 4b of the main content are involved with twisting in all three dimensions and the structure at small scale ($l=1.1 \mu\text{m}$) does not keep a linear relationship with the large-scale pinwheel ($l=2 \mu\text{m}$ in Fig. 3e). This makes it difficult to build a 100% replica model of the real 3D structures, especially at nanoscales. For ease of calculation and analysis, a simplified simulation model is built in fig. S9a-9b according to the SEM images of the structures fig. S9c, which is geometrically similar as that in Figs. 3a of the main text. As a result, the calculated magnetic field and electric current flows (in the center parts of the pinwheels) in fig. S7c, S7f and S7g, as well as the corresponding analysis, are well consistent with the illustration in Figs. 3b-3c of the main text, revealing the physical origin of the optical chirality. Meanwhile, the calculated transmission spectra of the 3D pinwheels are in agreement with the measured results, as shown in figs. S9d-9e. However, due to the minimum transmission caused by the Wood's anomaly at the wavelengths close to the lattice period of $1.45 \mu\text{m}$, the retrieved circular dichroism and circular birefringence show unrealistic peaks at this wavelength region, as shown in figs. S9f-9g. These unrealistic data are therefore not shown for clearance in the main text of Figs. 4d-4e.

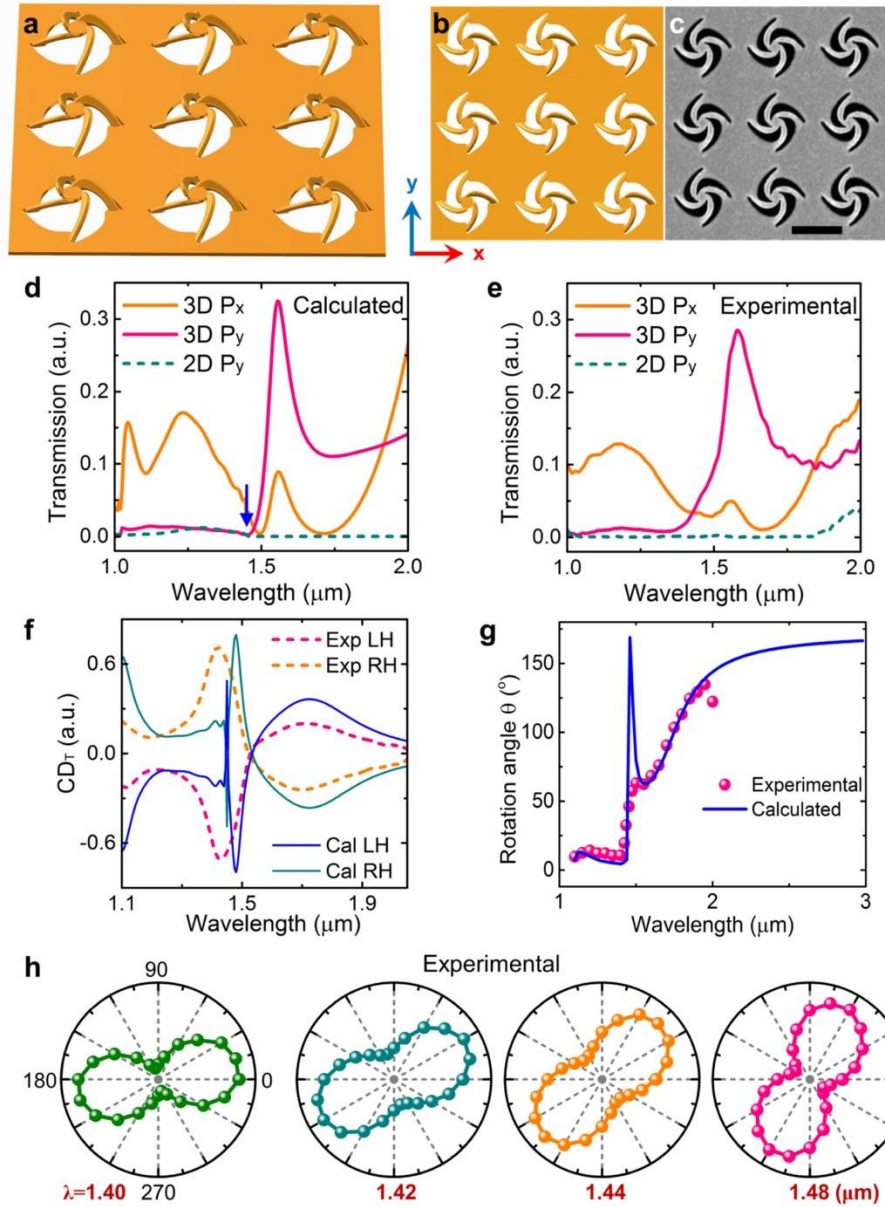


Fig. S9. Numerical calculations and comparison with experiments. (a and b) Side-view and top-view schematic of the 3D pinwheel in optical modeling, which is quite consistent with the top-view SEM image of the experimental 3D pinwheel in (c). (d, e) Calculated and measured transmission spectra of 3D and 2D pinwheels under detection with x-polarization (P_x) and y-polarization (P_y), respectively. The polarization of incident light is along x-direction. The blue arrow in (d) indicates the minimum transmission caused by the Wood's anomaly at the wavelengths close to the lattice period of $1.45 \mu\text{m}$. The spectra of LH 3D and 2D pinwheels under y-polarized detection are very different, revealing the tremendous changes brought by the nano-kirigami. (f) Experimental (Exp) and calculated (Cal) circular dichroism (CD) in transmission versus wavelength for 3D LH and RH pinwheels, respectively. To elucidate the effects brought by nano-kirigami and to rule out the background influence, here the CD is defined as $CD_T = (T_L - T_R)/(T_L + T_R)$. (g) Measured and calculated polarization rotation angle (θ) in anti-clockwise direction versus wavelength for a 3D LH pinwheel structure. Due to the inaccurate retrieve of polarization states at nearly zero transmission at Wood's anomaly, the spectra in (f) and (g) possess unrealistic sharp peaks around $1.45 \mu\text{m}$, which are not shown for clearance in Fig. 4 of the main text. (h) Polar-plots of experimental transmission versus detection polarization angle under x-polarized incidence. It can be seen that for wavelengths in the strong CD region (around $1.45 \mu\text{m}$), the transmitted light exhibits elliptical polarization states.

Section S3. Extension of nano-kirigami to other materials and geometries

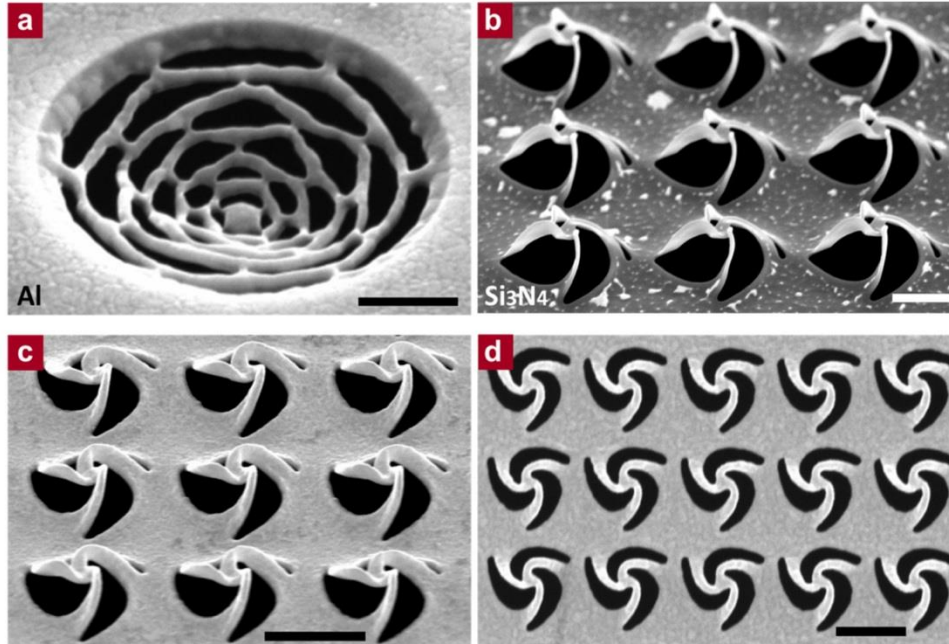


Fig. S10. Extension of nano-kirigami to other platforms. (a and b) Nano-kirigami enabled 3D structures in (a) a 100-nm-thick aluminum film and (b) a 50-nm-thick silicon nitride thin film. (c) Side-view and (d) top-view SEM image of three-arm 3D pinwheels fabricated in a 80-nm-thick gold film. Scale bars: 1 μm .

It should be mentioned that in this paper the residual stress distribution form in Eq. (7) is valid for gold nanofilm under gallium ion irradiation with high acceleration voltage of 30 kV. When using other materials or other types of ion beams, the distribution of vacancies and implanted ions will be different (as could be simulated by SRIM like in fig. S3) and the specific form of the residual stress distribution is therefore upon modifications. Nevertheless, the concept of employing topography-guided stress equilibrium for nano-kirigami is universal, which can be applied to a wide variety of free-standing thin-film materials. For example, a free-standing aluminum thin film with thickness of ~ 100 nm can be adopted with the topography-guided nano-kirigami (as shown in fig. S10a), although the buckling-up and buckling-down processes are quite different due to the tensile and compressive stresses of aluminum film are distinctive from those of gold (results not shown). In a similar way, commercially available silicon nitride films have also been successfully tested with our nano-kirigami method by initially coating a ultra-thin conductive gold layer, as the result shown in figs. S10b. The geometries of the functional 3D structures by nano-kirigami, as well, could be extended to other types such as a three-arm 3D pinwheel that breaks the center-reversal symmetry (figs. S10c-10d).